

Available at [www.sciencedirect.com](http://www.sciencedirect.com)

SciVerse ScienceDirect

journal homepage: [www.elsevier.com/locate/carbon](http://www.elsevier.com/locate/carbon)

# A comparison of Raman signatures and laser-induced incandescence with direct numerical simulation of soot growth in non-premixed ethylene/air flames

Jennifer D. Herdman <sup>a</sup>, Blair C. Connelly <sup>b</sup>, Mitchell D. Smooke <sup>b</sup>,  
Marshall B. Long <sup>b</sup>, J. Houston Miller <sup>a,\*</sup>

<sup>a</sup> Department of Chemistry, The George Washington University, Washington, DC 20052, USA

<sup>b</sup> Department of Mechanical Engineering, Yale University, New Haven, CT 06520-8284, USA

## ARTICLE INFO

### Article history:

Received 9 May 2011

Accepted 26 July 2011

Available online 31 July 2011

## ABSTRACT

The predictions of “soot” concentrations from numerical simulations for nitrogen-diluted, ethylene/air flames are compared with laser-induced incandescence and Raman spectra observed from samples thermophoretically extracted using a rapid insertion technique. In some flame regions, the Raman spectra were obscured by intense, radiation that appeared to peak in the near infrared spectral region. There is a good agreement between spatial profiles of this ex situ laser-induced incandescence (ES-LII) and the “traditional” in situ laser-induced incandescence (IS-LII). Raman signatures were observed from low in the flame and extended into the upper flame regions. The spectra consisted of overlapping bands between 1000 and 2000  $\text{cm}^{-1}$  dominated by the “G” band, near  $\approx 1580 \text{ cm}^{-1}$ , and the “D” band in the upper 1300  $\text{cm}^{-1}$  range. Several routines are explored to deconvolve the data including 3- and 5-band models, as well as a 2-band Breit–Wigner–Fano (BWF) model. Because the Raman signals were observed at heights below those where in situ LII was observed, we postulate that these signals may be attributable to smaller particles. The results suggest that the observed Raman signals are attributable to particulate with modest ( $\approx 1 \text{ nm}$ ) crystallite sizes. This observation is discussed in the context of current models for nascent particle formation.

© 2011 Elsevier Ltd. All rights reserved.

## 1. Introduction

In the combustion of fossil or bio-derived fuels under rich conditions, some fraction of the fuel carbon is converted into particulate carbon. This carbonization process most often leads to “soot”, a form of amorphous carbon characterized by small (10–30 nm) primary particles, with both crystalline and amorphous domains, aggregated into fractal structures. The formation of particulate carbon plays a critical role in energy generation (from the soot coating of furnace walls in a commercial boiler, to soot particle impingement on the tur-

bine blades of a commercial airline engine) and in the environment (from increasing mortality in urban areas to positive radiative forcing contributing to climate change).

Soot formation in hydrocarbon flames is kinetically controlled and occurs in short times (1–10 ms to reach particle diameters of 500 Å) [1]. This constraint of rapid particle formation limits the possible chemical processes that may form soot. Polynuclear aromatic hydrocarbons (PAH) have often been invoked as important intermediates in this chemistry. PAH are found in all sooting, hydrocarbon flames, have structures similar to the soot’s graphitic morphology, and posses

\* Corresponding author. Fax: +1 202 994 7474.

E-mail address: [houston@gwu.edu](mailto:houston@gwu.edu) (J.H. Miller).

0008-6223/\$ - see front matter © 2011 Elsevier Ltd. All rights reserved.

doi:10.1016/j.carbon.2011.07.050

C/H ratios between most starting fuels (<1) and soot particles (>5). Thus, they are often invoked as key intermediates in the chemistry that leads from fuels to soot.

Our understanding of carbonization during combustion is derived from experimental measurements near the beginning (through the measurements of concentrations of small, volatile molecular species) and at the end (in situ optical and/or microscopic analysis of collected particulate matter) of the process. As a consequence, key steps in the carbonization process are poorly defined including the relative abundance of aromatic and aliphatic carbons in the particles [2] and the mechanism for the transition from planar polynuclear aromatic compounds into three dimensional structures.

In several recent papers, other researchers and we have hypothesized that PAH agglomeration in flames occurs at modest molecular size [3–5]. Further evidence for the existence of these aggregates was postulated to be provided through the reassignment of the broadband laser-induced fluorescence that has been observed in soot-producing flames to excimer excitation [5]. Semi-empirical and density functional theory (DFT) calculations of electronic transitions for small aromatic aggregates were performed in support of this theory. Happold et al. have observed a series of peaks at molecular masses >650 Da when performing photoionization mass spectrometry on material sampled from a low-pressure ethylene/oxygen flame [6]. A reasonable explanation for their results is that the species responsible of these peaks are dimers (or larger aggregates) of smaller PAH.

Several groups in the soot community have postulated that early particulate matter is composed of aromatic ring systems joined by aliphatic linkages [7]. It has been proposed that initially these species form from reactions between small aromatic radicals and parent compounds or from aromatic radical recombinations. Dynamic simulations of the growth of these structures predict organic structures with 1–10 nm extents, but with seemingly lower density than graphitic carbon [7], lower aromatic conjugation lengths, and low sticking probabilities with each other at flame temperatures [8]. However, it has been reported that aromatic species with aliphatic side chains might aggregate faster than comparably-sized, fully-condensed PAH structures [9].

These two views present a stark contrast in the expected morphology for the youngest particulates formed in flames. As noted above our suite of diagnostics available to extract this morphological information is limited, particularly for atmospheric pressure flames. In this paper we combine for the first time two techniques that have been applied to analysis of particulate carbon: thermophoretic sampling and Raman scattering. Results of this analysis are compared with particulate concentrations determined by in situ laser-induced incandescence and with the results of direct numerical simulation.

## 2. Raman spectroscopy and microscopy of carbonaceous particulate

For more than 30 years, Raman spectroscopy has been used to characterize graphitic and amorphous carbon materials [10] ranging from graphite (>1000 references), urban particulate [11–13], and fullerenic materials including both single and

multiwalled nanotubes [14]. It has been applied to problems in atmospheric, environmental and geological chemistry [15–18], astrophysics studies of extraterrestrial carbon samples and meteorites [18,19], and in combustion studies of fuels, engines and their byproducts [20–26].

Because Raman scattering depends on the coupling between vibrational and electronic density of states, it is uniquely suited to be a probe of graphitization. It is surprising that few Raman studies of flame-generated soot have been presented [27], and many of these studies have focused on commercial or soot “standards” [28]. Thus, the samples may be free of their volatile components and may have undergone aging processes, including oxidation, that will change their morphology and thus their Raman signature [29].

One of the earliest studies of carbonaceous materials using Raman spectroscopy was in 1970 by Tuinstra and Koenig [10]. The Raman spectrum of a single crystal of natural graphite produced a single peak located at  $1575\text{ cm}^{-1}$ . Samples of charcoal, carbon black and glass-like carbon were also studied and these spectra produced this feature as well as another peak located at  $1355\text{ cm}^{-1}$ . In the Tuinstra and Koenig study, the intensity of the lower wavenumber peak was inversely correlated with crystal size which could be modified by grinding and analyzed through X-ray diffraction [10]. The  $1575\text{ cm}^{-1}$  peak (later to become known as the “G”, graphite, band) is assigned to the two  $E_{2g}$  modes, which are close enough in energy that they are indistinguishable. The other peak, with  $A_{1g}$  symmetry, at  $1355\text{ cm}^{-1}$  was initially called the “D”, or defect, band.

Invariably, large PAH also show transitions near  $1600\text{ cm}^{-1}$  and several near  $1300\text{ cm}^{-1}$  and DFT calculations of their electronic structure have been used to shed light on the origin of Raman spectra in larger systems [30]. It has been proposed that the D band in amorphous carbon arises from phonons localized in  $sp^2$  domains confined by disorders on the order of nanometers in size, the size of larger PAH [30]. Further, the width of the D band is attributable to the distribution of the  $sp^2$  domains sizes and shapes. Finally, the position of the G band, the ratio of the D band to G band intensities, and the line-width of the main line in the second order spectrum at  $2700\text{ cm}^{-1}$  have all been used to follow graphitization, specifically the two dimensional growth of  $sp^2$  domains and three dimensional ordering of adjacent planes [31,32].

A variety of approaches to the analysis of Raman spectra from carbon materials have been proposed. Sadezky et al. [23] optimized fitting parameters, including the number of bands (three, four or five) to be fitted, which line shapes to use, and suggested morphological information that could be extracted from the data. In this study, sixty-six experiments were performed using nine different carbonaceous samples and up to nine different fitting parameters based on the number of bands and line shapes for each band. The G and D1 bands are assigned to the  $E_{2g}$  and  $A_{1g}$  modes, respectively, as noted above. In their analysis, D1 was the most prominent band deconvolved from the D band and increased in intensity with the amount of disorder in the sample. The second defect band, D2, is slightly higher in energy than the G band and therefore appears as a shoulder of the G band. It is also attributed to  $E_{2g}$ , but originates from surface graphene layers [33]. It has been suggested that the D3 band represents amorphous

carbon within the soot sample, including adsorbed molecules or molecular fragments [23,34,35]. Finally, it has been suggested that the D4 band, usually observed as a lower energy shoulder of D1 and is also observed in glassy carbon [23,36], is due to  $sp^2$ - $sp^3$  bonds or vibrations from single and double bound carbons [23,27,37]. As noted below, this latter observation will depend on excitation energy.

An alternative approach to interpreting Raman signatures was initially suggested by Ferrari and Robertson [38] and has been discussed extensively in subsequent articles by their groups and other authors. Ferrari and Robertson suggest a simpler fitting protocol in which the D band is fit with a Lorentzian and the G band with a Breit–Wigner–Fano line shape

$$I(\omega) = \frac{I_0[1 + 2(\omega - \omega_0)/Q\Gamma]^2}{1 + [2(\omega - \omega_0)/\Gamma]^2} \quad (1)$$

where  $Q$  is a coupling coefficient that accounts for G band dispersion and  $\Gamma$  is a broadening coefficient. This equation approaches a Lorentzian band shape when  $1/Q \rightarrow 0$ .

Several reports have emphasized the correlation of Raman scattering and the electronic structure of the carbonaceous particulate. Raman spectroscopy using visible photons is  $\approx 100\times$  more sensitive to  $sp^2$  carbon sites than  $sp^3$  carbon sites because visible photons preferentially excite  $\pi$  states. (Only when the excitation energy exceeds  $\approx 5$  eV ( $\lambda < 250$  nm) are  $\sigma$  states probed.) Ferrari and Robertson noted that  $\pi$  states have minimum band gap energies given by:

$$E_g \approx \frac{2\gamma}{M^2} \approx 2\gamma \left( \frac{a}{L_a} \right) \quad (2)$$

where  $\gamma$  is a measure of  $pp\pi$  interaction,  $M$  is the number of aromatic rings in a cluster,  $a$  is the lattice spacing, and  $L_a$  is the in-plane crystallite size [38–40].<sup>1</sup> This prediction is largely borne out in the absorption spectra of PAH molecules, particularly those with aspect ratios near 1. From our analysis of the energy of the lowest allowed transitions for 33 PAH ranging in size from naphthalene (2 rings) to circumovalene (24 rings), we determined that  $\gamma = 2.42 \pm 0.17$  eV (Supplementary material). Thus, an excitation laser with a wavelength of 532 nm would have energy in excess of the band gap of a  $\approx 4$  ring PAH and a 785 nm laser would be expected to excite a  $\approx 9$  ring PAH. Assuming a lattice spacing of 0.35 nm, Eq. (2) predicts that the equivalent crystallite size,  $L_a$ , would be  $\approx 0.7$  and  $\approx 1.1$  nm, respectively.

The D peak is a breathing mode with  $A_{1g}$  symmetry that requires the presence of 6-membered rings, but is forbidden in perfect graphene sheets. Thus, it is indicative of disorder. For large graphitic clusters with relatively low disorder, the ratio of D to G Band intensities is inversely proportional to  $L_a$

$$\left( \frac{I_D}{I_G} \right) \propto \left( \frac{1}{L_a} \right). \quad (3)$$

This was the regime studied initially by Tuinstra and Koenig [10].

As disorder continues to increase, cluster sizes decrease and the number of  $E_{2g}$  interactions between pairs of  $sp^2$  car-

bons (that give rise to the G band) decrease. For these small clusters, with low  $L_a$ , the D-band intensity is proportional to the area of the aromatic domains of pericondensed, hexagonal ring systems:

$$\left( \frac{I_D}{I_G} \right) \propto L_a^2 \quad (4)$$

For both regimes of cluster size (Eqs. (3) and (4)), the constant of proportionality is an excitation wavelength-dependent factor. As noted above, the intensities of the Raman scattering features are connected with the relationship between the band gap of the material and the Raman excitation wavelength. In the case of large PAH, the pre-resonance and resonance Raman contributions to D band dispersion has been correlated with the number of conjugated  $sp^2$  carbons [41]. These results build on substantial earlier literature from the 1980s including the work of Knight and White [42] who showed a linear inverse relationship between  $L_a$  and  $I_D/I_G$  with a constant of proportionality,  $C$ , equal to 4.4 nm for the 514.5 nm argon ion laser line used in their study. Matthews et al. [43] studied the band area ratio,  $A_D/A_G$ , as a function of laser excitation wavelength using polyparaphenylene (PPP), glassy carbons, and carbon blacks. Their data suggested a linear relationship for the C-dependence on the excitation wavelengths (400 nm  $< \lambda_L < 700$  nm):

$$C(\lambda_L) \approx C_0 + C_1 \lambda_L \quad (5)$$

where  $C_0$  is equal to  $-12.6$  nm and  $C_1$  is 0.033. Although these values are based on PPP data, a linear relationship was found for all of the samples studied. Data presented in Sadezky et al. [23] also show a linear dependence of  $I_D/I_G$  and extend the excitation wavelength farther into the infrared with an almost identical slope and intercept. Using this correlation and for excitation at 785 nm, we estimate the value of  $C$  to be 13.31 nm.

To maintain continuity between the two regimes of cluster size, the  $I_D/I_G$  ratio has been anchored at a value of  $L_a = 2$  nm [44]. This leads to a constant of proportionality for small clusters (Eq. (4)) of  $1.66 \text{ nm}^{-2}$  at 785 nm. (We will refer to this constant as  $C'$  to maintain consistency with Ferrari and Robertson [38]).

Until recently, there has been little literature that supports the intensity ratio trend for low crystallite size (Eq. (4)) or locating the magnitude of the crystallite size at 2 nm for the maximum  $I_D/I_G$  ratio. Lucchese et al. presented results for the evolution in the Raman spectra observed with 514 nm excitation as a graphene sheet is bombarded with argon ions [45]. Scanning tunneling microscopy measurements of the samples during bombardment provided an independent measure of defect density. From this, a phenomenological relationship between  $I_D/I_G$  and  $L_a$  is derived that fits their data for particles with defect lengths ranging from  $<1$  nm to  $>20$  nm. In a more recent collaboration between this group and Ferrari, the same trend was observed when exciting at different laser wavelengths [45]. In the latter, this relationship is given by

<sup>1</sup> Various authors have used different titles for this variable including “in-plane crystallite size”, “correlation length”, and “conjugation length”. In all cases, we understand it to refer to the same concept: the characteristic dimension of the planar  $\pi$  system. For brevity, we will refer to it as the crystallite size in this manuscript.

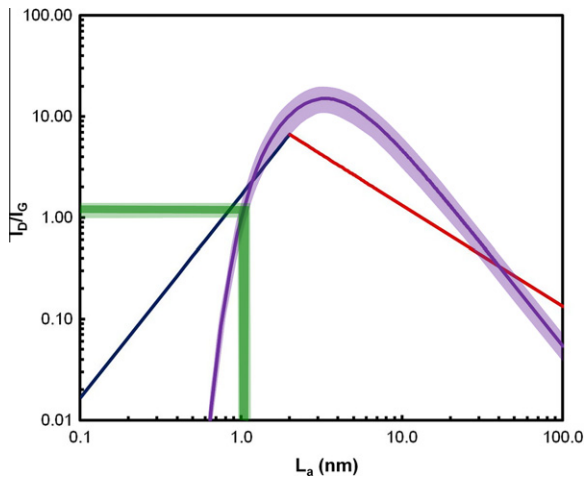


Fig. 1 – Adaptation of Zickler et al. (Ref. [44]).

Figure illustrating the relationship between the  $I_D/I_G$  and  $L_a$  for a 785 nm excitation laser source. Eq. (4) predicts that for particles with  $L_a$  less than 2 nm,  $I_D/I_G$  is proportional to  $L_a^2$  (blue line). For those greater than 2 nm, Eq. (3) predicts that  $I_D/I_G$  is proportional to  $L_a^{-1}$  (red line). More recent literature from ion bombardment of graphene sheet suggests the purple curve of Eq. (6). (The lighter shaded region represents the uncertainty in  $C_A$  at 785 nm.) Finally the green shaded area region shows the range of  $I_D/I_G$  observed in the present work (Section 4). (For interpretation of the references to color in this figure legend, the reader is referred to the web version of this article.)

$$\frac{I_D}{I_G} = C_A \frac{(r_A^2 - r_S^2)}{(r_A^2 - 2r_S^2)} \left[ e^{-\pi r_S^2/L_A^2} - e^{-\pi(r_A^2 - r_S^2)/L_A^2} \right] \quad (6)$$

where  $r_A$  and  $r_S$  are length scales that define the region in which D scattering occurs, and are reported to be 3.1 and 1.0 nm, respectively; values that fit their data and have precedence in the literature.  $C_A$  is a unitless, excitation wavelength-dependent factor and represents the maximum value of the  $I_D$  to  $I_G$  ratio. Note that Cancado et al. had previously suggested that this factor should depend on the laser excitation wavelength as  $E_L^{-4}$  [46] and the data in Ref. [47] supports this earlier result with

$$C_A = (160 \pm 48 \text{ eV}^4) \cdot E_L^{-4} \quad (7)$$

Fig. 1 summarizes the dependence of the  $I_D/I_G$  ratio on  $L_a$  for excitation at 785 nm, the Raman excitation wavelength used in this study. Shown are the generalized relationships characterizing the  $I_D/I_G$  ratio for small clusters (Eq. (4)), large clusters (Eq. (3)) as well as the data for graphene sheets (Eq. (7)). For the latter, shading represents the uncertainty in  $C_A$  expected with 785 nm excitation.

### 3. Experimental

#### 3.1. Burner and flame description

Two identical burners have been constructed for experiments at the George Washington University and at Yale University. In each, a fuel mixture of ethylene and nitrogen flows through a 0.4 cm inner diameter vertical tube, and air issues from

the annular region between this tube and a 7.5 cm inner diameter concentric tube. Flames with different fuel mixtures, composed of ethylene and nitrogen, were studied with ethylene concentrations of 32, 40, 60, and 80 vol.%. For all flames, the fuel velocity at the burner surface was a parabolic profile with an average velocity of 35 cm/s and air velocity profiles at the burner surface were plug flow of 35 cm/s; physically this was realized by having a honeycomb cover the region of co-flowing air. The flame was unconfined, and the flow was laminar. Electronic mass flow controllers, with long-term accuracy to within 5%, governed the flow rates.

#### 3.2. *in situ*, laser-induced incandescence

Experimental data quantifying the soot volume fraction were obtained using two-dimensional laser-induced incandescence (LII) measurements [48–51] calibrated with an on-line extinction method [52]. Both the LII excitation and the extinction calibration used a frequency-doubled Nd:YAG laser (532 nm), with the beam focused into a sheet across the centerline of the burner. A laser fluence of approximately 0.3 J/cm<sup>2</sup> was used for the LII measurements since, in this range, the detected signal was independent of small variations in the laser sheet profile and beam extinction across the flame did not result in a loss of signal. The LII signal was captured using a fast-gate (10-ns response time) intensified CCD camera. A gate time of 23 ns was used, with the intensifier fully on upon arrival of the laser pulse. A broadband filter centered at 405 nm with a bandwidth of 70 nm was placed in front of the camera. Detection at this blue-shifted wavelength minimized fluorescence interference and provided results that were in agreement with subsequent measurements made using 1064 nm excitation [53]. The raw LII images were averaged and corrected for luminosity and optical throughput. These images were further corrected for a left–right nonuniformity characteristic of the fast-gate intensifier and the 10-mm data slices were then combined to generate composite soot volume fraction images covering the entire flame.

The extinction calibration was carried out at a laser fluence of less than 0.01 J/cm<sup>2</sup>, low enough to avoid unwanted LII effects and altering the properties of the soot. The laser beam was separated by a beam splitter into an extinction beam, which follows the same path through the flame as the LII beam, and a reference beam, which does not traverse the flame. After it is partially extinguished by the flame, the extinction beam is re-collimated, and the extinction and reference beams are then aligned so that they travel parallel to one another, but at different heights. The two beams are focused into sheets by a cylindrical lens, and are incident on a dye cell containing a mixture of Rhodamine 640 and ethanol. The fluorescence of the dye cell is imaged by a CCD camera through a long-pass filter at 570 nm, which filters out light scattered from the incident laser. The relative intensities of the extinction and reference beams are used to determine how much of the laser is extinguished by the flame. The average soot volume fraction across the flame diameter is then determined using the Lambert–Beer law in the Rayleigh approximation [50], and the result is used to calibrate the LII images. Here, the dimensionless soot extinction coefficient

is taken to be 8.6 [54,55], which is the same value used for the numerical calculations. The on-line extinction calibration was performed only on the higher concentration flames (80% and 60% ethylene), and the results were extrapolated to the lower concentration flames (40% and 32% ethylene), since uncertainties in the calibration of the lower concentration flames began to dominate when the total extinction dropped below a few percent.

### 3.3. Raman spectroscopy and *ex situ*, laser-induced incandescence

Beginning with the pioneering work of Dobbins and Megaridis in the mid 1980s [56], thermophoretic sampling has become one of the standard tools for particle analysis in high temperature particle-forming systems. Typically, a sample holder such as a transmission electron microscope grid is rapidly inserted into a high temperature region. Because the target is initially cool, particles are deposited onto it during its brief residence time in the flame. In our lab, samples were collected on a horizontal,  $\approx 250 \mu\text{m}$  NiChrome wire that was rapidly inserted into the flame using a pneumatic piston (Fig. 2). The design of the sampling system is loosely based on the constant-tension rake design of Cundy et al. [57]. The rake plate (inset, Fig. 2) is attached to the end of a 12" construction rail (ThorLabs XE25L12) using an optical mounting base (ThorLabs BA1). This rail is attached to the top the pneumatic slide (Omega DLM-09M-50-50-P) using two 1" construction cubes (ThorLabs RM1G). This pneumatic slide (seen extended in Fig. 2) has a travel range of 2". The compressed air is introduced into the slide through 0.25" polyethylene tubing connected to flow control valves (Omega OM-AIR-C2VA0045). Insertion and retraction processes were driven by toggling pressurization/venting using a solenoid (Omega SV3110DC)/relay (Omega SSR330DC10) system controlled by a National Instruments DAQ SCB-68 through a LabView program.

The pneumatic sampling rig was mounted on a two-dimensional, position-encoded XY Scanning Stage (ThorLabs MAX203) connected to a stepper motor controller (ThorLabs BSC102) controlled by APT software. The horizontal positioning stage is attached to a vertical stage (z axis) that can travel a distance of 20 cm with a precision of 0.001 mm and is used for manual sampling height adjustment. Typically, the wire was held at the sampling position in the flame for  $<1$  s. Once a sample was collected, the wire was translated into the focal volume of a Kaiser Optical System, Inc. probe. The probe was aligned vertically and pointing upwards to allow for spectra to be obtained from samples collected on the bottom of the wire. Spectra were collected across the wire starting 2–3 mm outside the deposition area on one side of the flame and were continued across the wire in 0.1 mm steps to a comparable distance past the deposition region on the opposite flame annular region. Samples were taken at multiple heights above the burner (HAB) beginning at 4 up to 56 mm, where no Raman spectra were observed, in steps of 2 mm.

A concern that has been raised in the thermophoretic literature is the loss of spatial resolution that accompanies vibration during the sampling process. For example, in a recent paper in the Journal of Aerosol Science, a damping mechanism was engineered to minimize vibration during the rapid insertion process [58]. In our design, the long arm that supports the sampling rake is made of an extruded aluminum material (Thorlabs XE25) that we use in many of our optical designs, including a homemade confocal microscope, and have found it very stiff. We have performed our own visualizations of probe movement including following oscillations at the end of the insertion. For these measurements, we used a high definition movie camera operating at 60 frames per second. We examined the images frame by frame and followed the coordinates of several points on the rake. The vertical and horizontal position data were fit to a damped sine

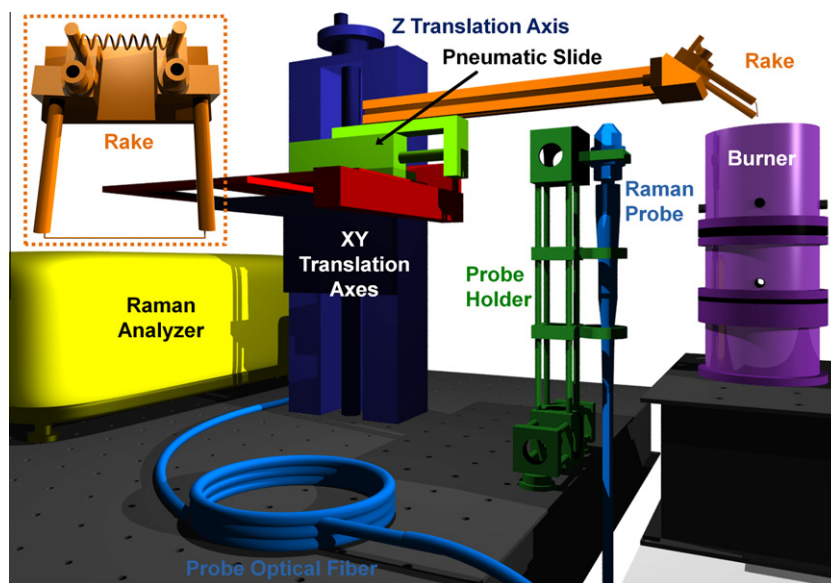


Fig. 2 – Experimental setup for Raman scattering measurements with the pneumatic slide shown in the extended position. The inset is a close up of the rake. One of the arms is loosely tightened so that the spring can compensate for any wire expansion or contraction to avoid sagging or breakage.

wave (Supplementary material). There was considerable consistency in the parameters of the fits, notably the magnitude of the initial oscillation was  $<0.5$  mm and this damped out with a characteristic time of about 0.3 s. Oscillations in the horizontal direction were substantially less. When our data is compared with data shown in Fig. 5 of the J. Aerosol Science article, vertical oscillations in their un-damped probe were much larger than ours and still greater than ours after the installation of their damping design.

Samples were excited with a Invictus, 785 nm laser and scattered radiation was analyzed with a RamanRxn1 Analyzer (both from Kaiser Optical Systems, Inc.) and the HoloGRAMS Software package. Up to 400 mW of power was available at the focal point of the probe. For many samples at high laser powers, a significant red-shifted emission was observed that overwhelmed the Raman scattering signal. We refer to this signal as “ex situ, laser-induced incandescence” (ES-LII) and will discuss it further below. To minimize the observation of ES-LII, the measurements reported below were collected using only 10 mW of laser power and a single scan at an exposure time of 25 s. Fig. 3 shows an example of collected spectra illustrating a Raman spectrum free of ES-LII (C), one with Raman scattering emerging from the ES-LII background (B), and one with only ES-LII apparent (A). The Raman spectrometer automatically corrects for wavelength dependencies of dispersion elements and detector response and produces a flat, near zero baseline. However the ES-LII signal required correction for broadband emission that was accomplished by fitting the background to a third order polynomial. The magnitude of the baseline signal in the spectral region of the Raman features is quantified below as the ES-LII signal. When Raman scattering was observed above this baseline, the baseline was subtracted, and the residual spectra were fit using two bands (D and G with BWF line shape, as described above); three bands (D1, D3, and G); or five bands (D1–D4 and G) using a Simplex algorithm coded into a Delphi (PASCAL) computer program. Fig. 4 shows typical fits using 2, 3, or 5 band models.

### 3.4. Numerical simulation

The computational model solves the full set of steady, elliptic, partial differential governing equations for mass, momentum, species and energy conservation [59]. The modified vorticity-velocity formulation in [60] is used to compute the velocity field as it is more effective at conserving mass than the original formulation [61]. The Soret and Dufour effects are neglected, and a model for Fickian diffusion is used. The diffusion model employs mixture averaging and a correction velocity that satisfies a mass conservation constraint [62]. All thermodynamic, chemical, and transport properties are evaluated using CHEMKIN [63,64] and TPLIB [65,66] subroutine libraries, parts of which have been rewritten and restructured for greater speed [67].

As the problem is cylindrically symmetric, the governing equations are solved over a two-dimensional mesh, bounded by an inflow plane, an axis of symmetry, an outflow plane at  $z = 25$  cm, and a far field boundary condition at  $r = 7.5$  cm. The inflow boundary condition specifies axial velocity, ambient temperature and species concentrations of either fuel or air. The radial velocity is set to zero and the vorticity is defined

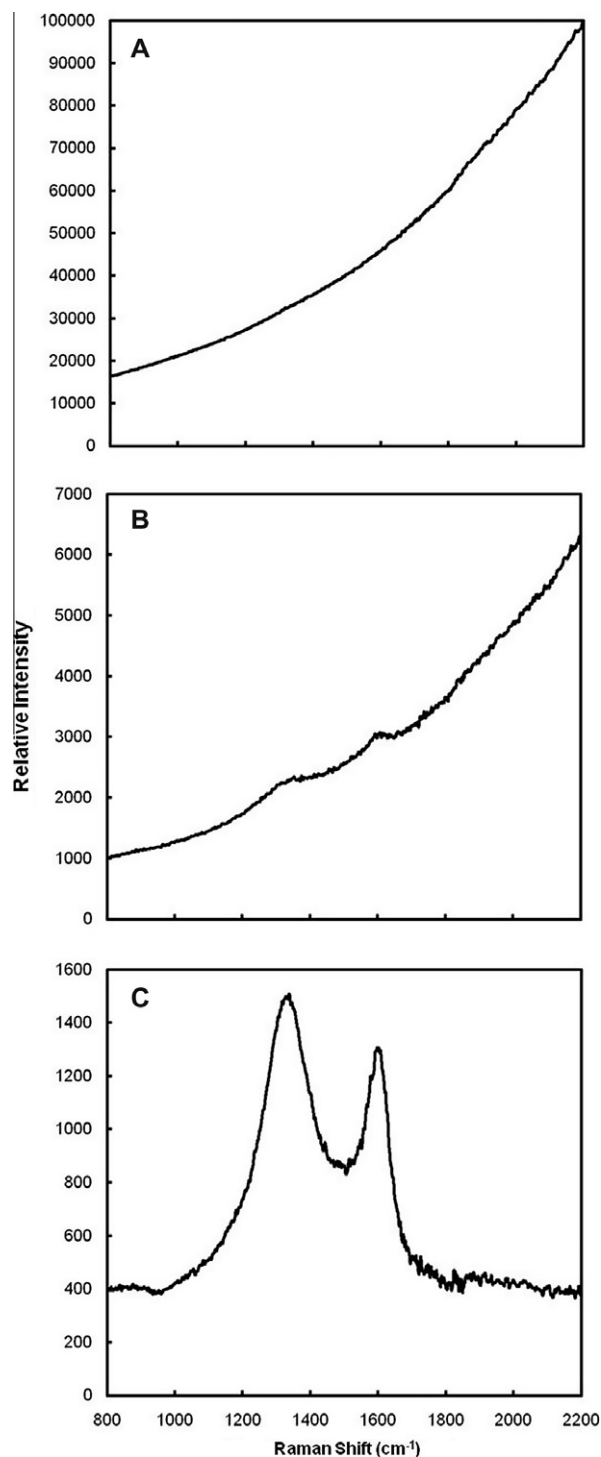


**Fig. 3** – Three types of emission/scattering spectra observed in the flame, ES-LII only (A), ES-LII and D and G bands (B), and spectra with only D and G bands visible (C). Note the difference in relative intensities of the y-axes.

as the curl of velocity. They symmetry boundary condition specifies zero radial velocity, zero vorticity and zero radial derivatives of all other variables. The outflow boundary condition assumes fully developed flow and sets all axial derivatives to zero. The far field boundary condition is specified using the continuity equation, the definition of vorticity, and

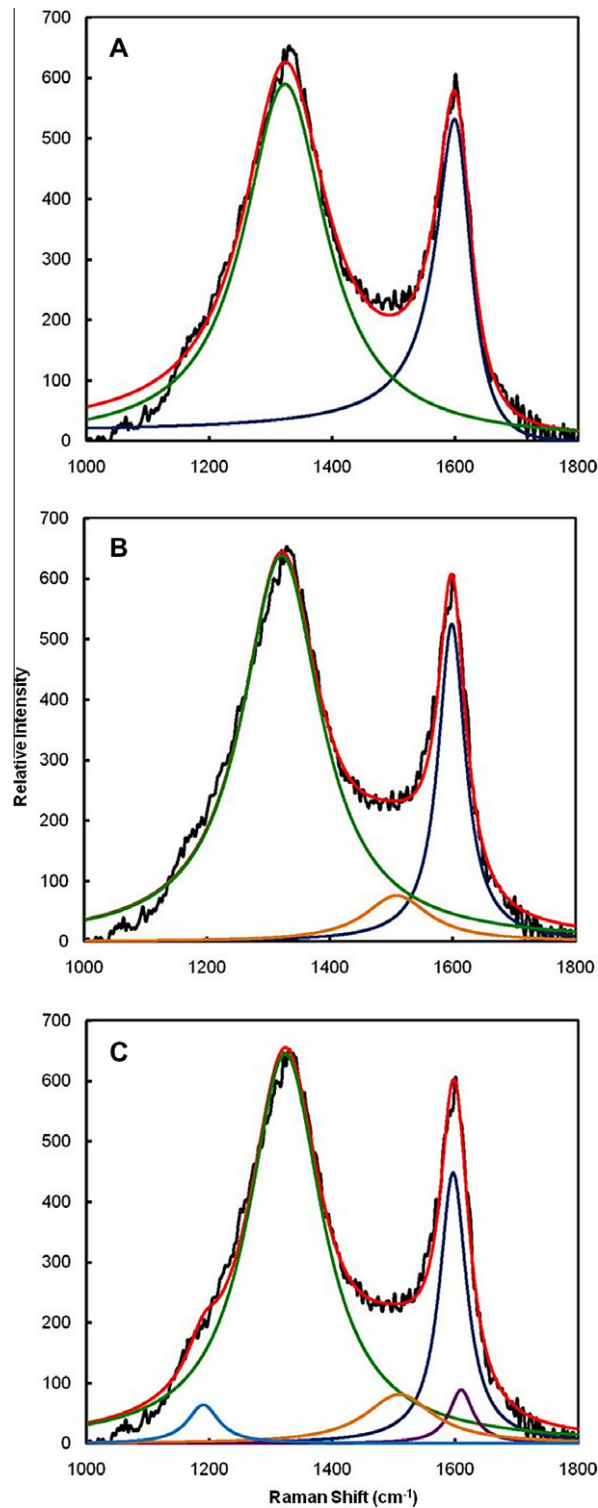


**Fig. 4** – Three different fitting schemes investigated to deconvolve Raman spectra: D1 (Lorentzian) and G (BWF) two-band fit (A); D1, G (Lorentzian), and D3 (Gaussian) three-band fit (B), and D1, D2, D4, G (Lorentzian) and D3 (Gaussian) five-band fit (C). In each panel are shown the raw data (black), fit spectrum calculated by summing the individual peak contributions (red), and the individual peak contributions [D1 (green), D2 (purple), D3 (orange), D4 (light blue) and G (dark blue)]. (For interpretation of the references to color in this figure legend, the reader is referred to the web version of this article.)

the condition that radial derivatives of axial velocity, temperature and species vanish. All other boundary conditions are

discretized according to the framework for mass conservation presented in [60].

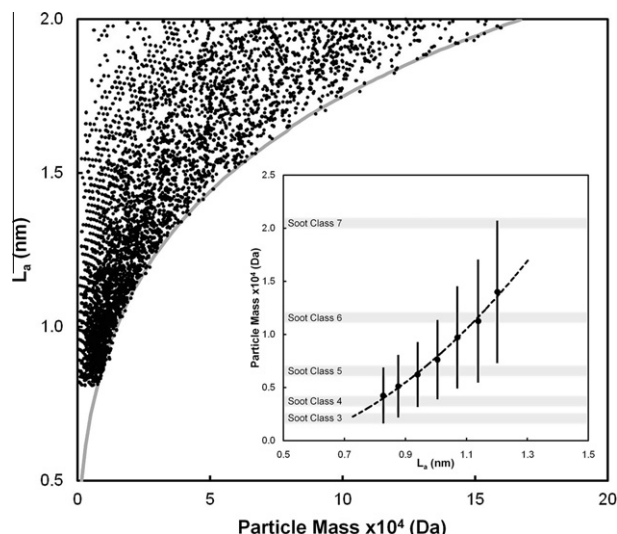


**Fig. 5 – Results of Monte Carlo simulation of particle morphology. (Only 10,000 trials are shown). The gray curve is an empirical fit of the lowest crystallite size found for a particular particle mass. The inset shows the low mass end of these trials with the axes transposed. Average mass for particles with an average crystallite size are shown as points. The vertical lines indicate the standard deviation in these masses. Superimposed on the mass axis are approximate bounds for several of the soot sections.**

The soot volume fraction was predicted using a sectional representation as discussed in greater detail in [68,69] and has been employed in a number of flame studies (e.g., [70–74]). It assumes that soot particles can be approximated as carbon spheres and that they exist in the free molecular limit (i.e., the mean free path of the gaseous mixture is much larger than the largest soot spheroid). The approach specifies a minimum and maximum particle mass and divides the spheroid sizes logarithmically into Nsec bins or sections. A further assumption is that within a given section, spheroids of varying diameter do not exhibit vastly differing aerosol dynamical qualities. This assumption holds as long as Nsec is sufficiently large. In the computations presented herein, a total of 30 soot sections (each soot section introduces an additional partial differential equation) was employed. Each soot section equation contains a balance among convection, diffusion and soot production/destruction. The soot production/destruction terms are formed from a combination of inception, surface growth and oxidation. The surface growth model used in the numerical simulations was based on the premixed flame data of Harris–Weiner [75] where we assumed an activation energy of  $E_s = 31.8$  kcal/mol [76].

The chemical mechanism was derived from one of the more comprehensive and well-validated sets available for ethylene [77]. It considers  $C_2H_4$  chemistry and includes reactions pertaining to small aromatic species, but nitrogen chemistry has been removed. The reaction set involves 66 species and 476 reversible reactions. The result is a model that requires a total of 100 dependent variables (66 chemical species equations, 30 soot sectional equations, an energy equation, two velocity equations and a vorticity equation) to

be solved at each grid point. The system is closed with the ideal gas law. The governing conservation equations are solved on a two-dimensional mesh by combining a Newton-based steady-state and a time-dependent solution method [73]. A time-dependent solution is first obtained on a coarse grid and then grid points are inserted adaptively to increase the resolution in regions of high spatial activity (see also [59]). Computations were performed on a 3.0 GHz Intel Xeon processor system with 8 cores per node and 16 GB RAM per node.

### 3.5. Estimating morphology within soot classes

As noted in the introduction, both the Raman excitation process and the appearance of the resulting spectra are highly dependent on the morphology of the carbonaceous material; in particular the distribution of aromatic structures within. The soot sectional model follows only mass distribution within each class. To provide an analysis of morphology within each class, a calculation was performed to evaluate plausible distributions of particle structures. In this model, we assume that soot particles are aggregates of PAH molecules. We begin with a set of aromatic molecules that include an integer number of aromatic rings between 1 and 50 rings (see Supplementary Material for representative structures). These species have a range of C/H ratios between 1 and  $\approx 6$  and follow the Stein–Fahr “stabilomer” grid [78]. These molecules are a class of thermodynamically-stable, condensed-ring molecules that have been observed in laser-desorption measurements of nascent soot particles in both premixed and non-premixed flames [79,80]. A Monte Carlo algorithm was used to construct particles from these PAH species. For each particle simulated it was assumed that the PAH that comprise the particle followed a log normal distribution as has been observed in PAH gas phase condensation experiments [81]. For each particle, the mean of the log normal distribution was allowed to vary randomly between  $e^{5.5}$  and  $e^{7.0}$  (245–1097 Da) and the standard deviation of the distribution between 0.1 and 0.6. The low end of this mass range represents the smallest PAH that have been invoked for non-bonded interactions leading to soot nuclei [82,83]. In addition, a random intensity factor was applied to the particles distribution function leading to particles with overall mass ranging between  $\approx 10^3$  and  $\approx 10^5$ . The number of each PAH represented in the particle was rounded to the nearest integer. Once a particle was constructed, a weighted average aromatic correlation length was calculated for the particle by evaluating Eq. (2) for each PAH in the particle and then normalizing by their respective populations.

## 4. Results and discussion

The aim of this work is to correlate the observation of both Raman and LII (both in situ and ex situ) with the direct numerical simulation of molecular growth chemistry. To begin this discussion, we will present the results of the Monte Carlo simulations of particle morphology that will aid in predicting plausible morphology limits within the predicted soot classes. We will then present results showing qualitative agreement between predicted and measured spatial profiles for all three experimental signatures. Finally, we will

discuss these results in the context of existing models for interpretation of both LII and Raman signatures from carbonaceous particulate.

#### 4.1. Results of Monte Carlo simulation

Fig. 5 presents the results of  $\approx 10,000$  (of the 500,000) Monte Carlo trials plotted with average PAH correlation length,  $L_a$ , shown as a function of particle size. The results show a broad spread in these quantities. However some generalizations may be made. First, only the smallest particles (<10 KDa) have average correlation lengths lower than 1 nm. This range of small particles would be expected to have spherical equivalent particle diameters  $\leq 2.5$  nm (assuming a density of  $1.5 \text{ g/cm}^3$ ) and would encompass the first 5 soot classes in the direct numerical simulation (Section 3.4), as shown in the inset of Fig. 5. As particles grow in mass, so does the average crystallite size. For each mass, there appears to be a minimum calculated crystallite size, indicated by the empirical curve in Fig. 5 that has the formula:

$$\bar{L}_{a,\min} = 4.0867 \times 10^{-2} \cdot \ln(M_{\text{particle}})^2 - 4.7534 \times 10^{-1} \cdot \ln(M_{\text{particle}}) + 1.7994 \quad (8)$$

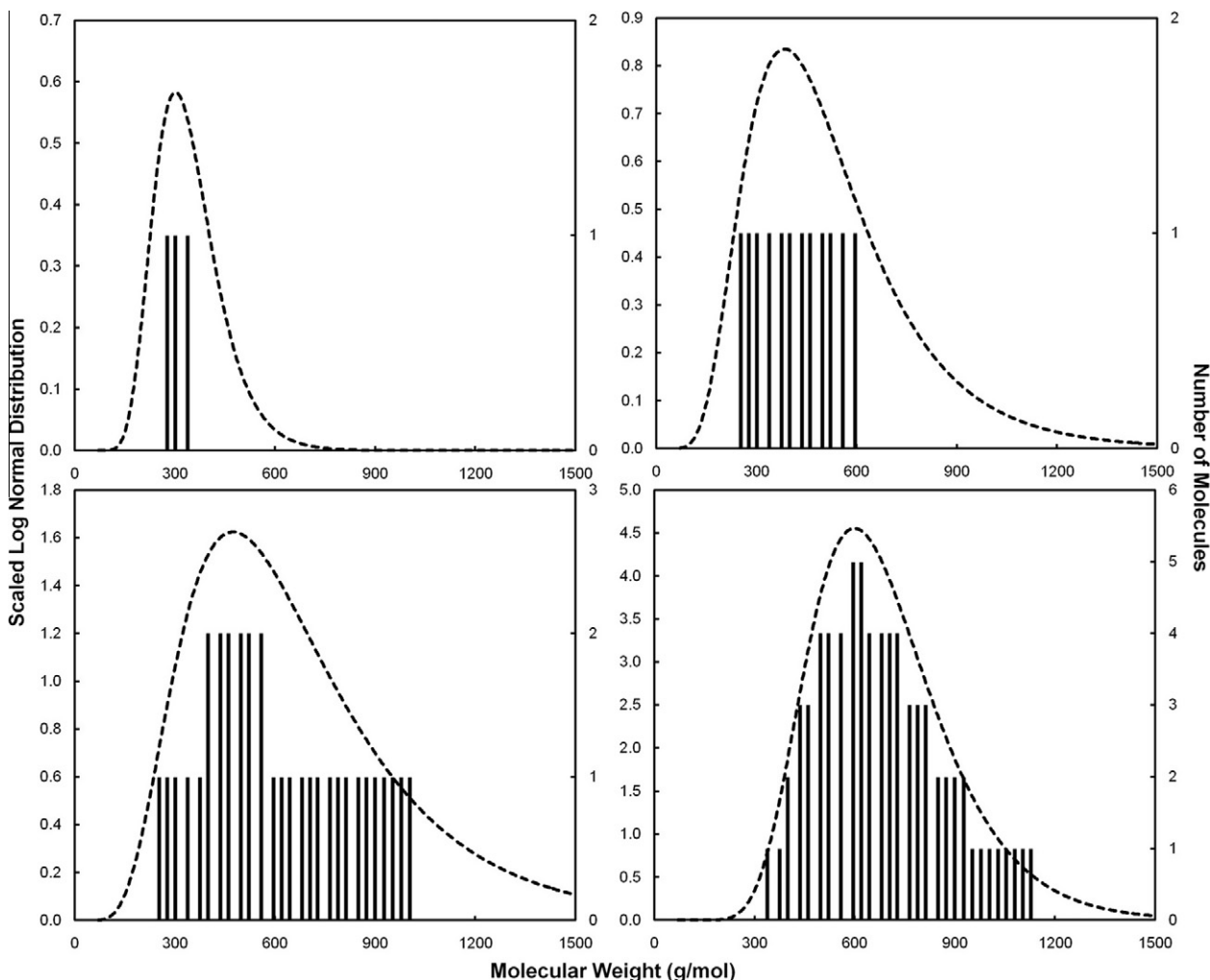


Fig. 6 – Several representative distributions of PAH within some calculated nascent particles. The dashed line shows an ideal log-normal distribution of masses. The vertical bars show the corresponding rounded population distributions.

Fig. 6 shows a few distributions from these trials representative of particles with mass of approximately 1000, 5000, 20,000, and 50,000 Da and containing 3, 12, 33, and 73 PAH molecules, respectively. For each trial, both the calculated log normal distribution function is shown as well as the discrete PAH composition.

These computational results suggest what might be intuitively obvious: the smallest soot particles are composed of relatively few PAH and have low average crystallite size. Because crystallite size is inversely correlated with optical band gap energies, these small particles are expected to have large band gaps. This fact may have implications for both the interpretation of LII signals as well as Raman spectra. Larger particles are composed of more and, on average, larger PAH and thus have lower band gaps.

#### 4.2. Comparison of LII and predictions of soot class

Fig. 7 shows a comparison of flame temperature, the calculated sum of the concentrations of all soot classes with  $N \geq 3$  (Section 3.4), and the measured in situ LII signal. This lower limit for the summation of soot classes was chosen because 532 nm excitation is expected to exceed the optical

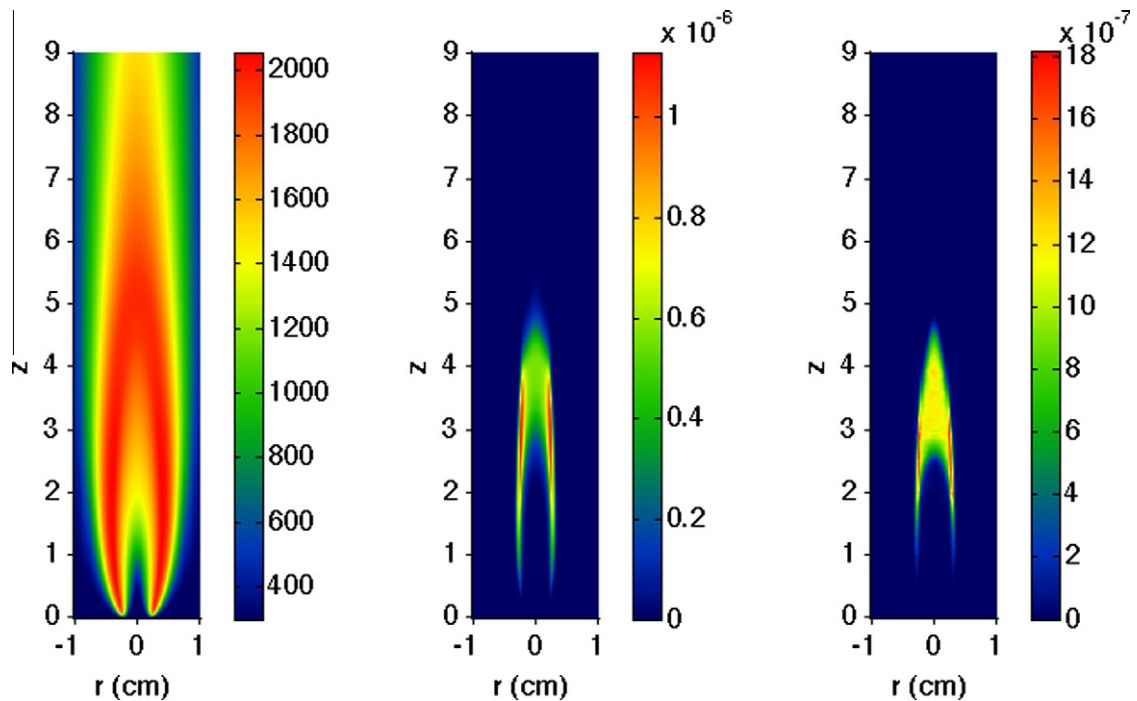


Fig. 7 – Contours of computed flame temperature, the calculated sum of the concentrations of all soot classes with  $N \geq 3$  (Section 3.4), and the measured in situ LII signal.

band gap for particles of approximately this size (Supplementary material). As noted previously, there is an evolution in location of peak soot volume fractions from the more dilute to less dilute flames (see Supplementary material for addi-

tional comparison of profiles). As the nitrogen concentration in the fuel stream decreases, the flames lengthen and the peak soot shifts from being located near the axis of symmetry to annular regions. The majority of the Raman/ES-LII

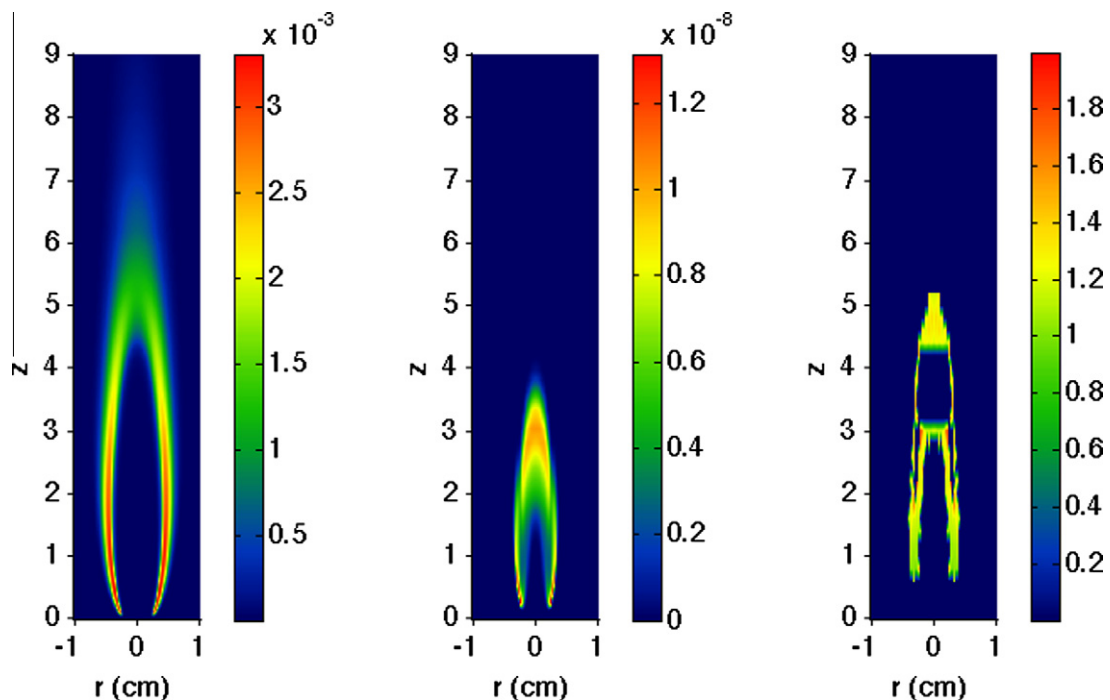


Fig. 8 – Contours for computed hydroxyl radical, the sum of calculated soot classes 3 through 7, and the observed ratio of  $I_D/I_G$  in regions where Raman scattering was observed and could be quantified over the ex situ LII signals. For clarity in the last panel, regions where ES-LII dominated Raman in the middle of the flame are shown in dark blue. (For interpretation of the references to color in this figure legend, the reader is referred to the web version of this article.)

sampling was done in the 60% flame. However, limited sampling at 10, 20, 30, and 40 mm HAB in the other three flames showed similar patterns. Specifically, signals were only observed at 20 mm in the 32% flame, 10, 20, and 30 mm in the 40% flame, and all four heights in the 80% flame. Results from the 60% flame are described in more detail below.

#### 4.3. Raman, *ex situ* LII, *in situ* LII

Fig. 8 presents contours for hydroxyl radical, the sum of soot classes 3 through 7, and the ratio of  $I_D/I_G$  in regions where Raman scattering was observed and could be quantified over the *ex situ* LII signals. The  $I_D/I_G$  ratio varies only slightly whenever Raman is observed; from a low of approximately 1.0 to a high value of 2.0, with the vast majority of the data observed between 1.0 and 1.4. Referencing the correlations presented in Fig. 1, this implies a crystallite size,  $L_a$ , varying from  $\approx 0.8$  to 1.0 nm for the correlation defined in Eq. (4) or 1.0–1.2 nm considering Eq. (6) and the associated uncertainties in  $C_A$ . Given the recent availability of experimental data for this small crystallite size regime [45], the latter correlation likely provides a more accurate picture.

The inset of Fig. 5 presented results from the Monte Carlo simulations for small clusters and compares them with approximate size range of some early soot classes. As the middle panel in Fig. 8 suggests, there is a reasonable agreement between the extents of this young soot and the observed Raman signals near the base of the flame. The agreement is not as good higher in the flame ( $>4$  cm) where Raman signals continue to heights above those where substantial concentrations of small soot particles are calculated. As this is a region where oxidation of carbonaceous particulate by hydroxyl radical is expected to occur, the presence of carbonaceous Raman scatterers here suggest particle break-up that is not well captured by the sectional soot model.

As noted above, the heavier soot-bearing regions produced what we believe to be a laser-induced incandescence signature. This signal was strongly dependent on laser power and could be minimized, but not eliminated by lowering the delivered power (see [Supplementary material](#)). Similar emissions have been reported by others and has also been termed a fluorescence continuum [84] or “high fluorescence” [85]. Ivleva et al. attributed their observations of “high fluorescence” found in air particulate to organics, both biological and those found in soot, specifically PAH [85]. In Brunetto et al.’s 2009 publication, they attributed this feature to aromatic-rich soot because of the more accessible  $\pi$  excitations that are absent in aliphatic-rich soot, which does not produce a similar feature [84]. In a recent paper, similar signals were observed in single walled nanotubes [86] and the authors were able to determine a temperature from the near infrared emission spectrum which, depending on laser wavelength and power, were in the 1000–1500 K range. This literature, combined with our observations of the spatial overlap of regions in the flame where particles are seen by *in situ* LII and the broad emission is observed in the thermophoretically sampled material argues that these are phenomenologically similar. That is not to say that there is not a morphological basis for these observations; it is likely that near infrared photons are more likely

absorbed by the larger aromatic structures within either *in situ* or extracted carbonaceous material.

Finally, we return to the subject of insights available from interrogation of Raman band structure. We were initially surprised to find such little variation in the Raman spectra collected throughout these flames. However, these observations can be rationalized within the context of current models for soot growth. Frenklach and Wang followed the evolution of size in a model for soot growth that includes both chemical growth through the “HACA” mechanism and physical coagulation of PAH [87]. They found that particle size was determined primarily by the latter and that the size of PAH did not vary throughout the particle inception zone. In recent modeling work of the Kraft group at Cambridge University, Totton et al. evaluated early soot particulate morphology on the basis of PAH aggregation energetics [88]. They conclude that a cluster of PAH molecules as small as coronene provides a reasonable model for a nascent soot particle [89]. In a more recent publication from the same group, simulations of the chemistry and physics that lead from isolated PAH to primary particles was investigated. Histograms of PAH size distributions within a primary particle are reported and show a large abundance of small PAH (25 carbon atoms) for both smaller and larger primary particles [90]. As discussed above the ratio of  $I_D/I_G$  varied little in observed Raman spectra. Correlations of this quantity, for 785 nm excitation, with crystallite size suggest variations in the latter over a narrow range of  $\approx 1.0$ –1.2 nm. As a hexagonal aromatic ring is  $\approx 0.25$  nm across, the lower end of this range would be equivalent to PAH that are 4–5 rings across (approximately the size of circumcoronene). The data suggest that the Raman signal we observe is consistent with nascent particles that have a morphology dominated by modestly-sized PAH with masses in the 500–1000 Da range.

Our experiments cannot shed light on the crystallite size of material collected from flame regions where ES-LII dominates Raman scattering. Sander’s et al.’s work [89] suggests that little change might be expected since primary particle size as well as the aggregation of these particles into fractal structures are dominated by physical processes rather than edge growth of aromatic regions which would result in a crystallite size and thus a larger  $I_D/I_G$  ratio. Finally, because the Raman spectra of material collected from the oxidation regions higher in the flame have similar  $I_D/I_G$  ratios, understanding morphological changes that accompany particle destruction presents an opportunity for both modelers and experimentalists.

---

## 5. Conclusions

The predictions of “soot” concentrations from numerical simulations of a series of nitrogen-diluted, ethylene/air flames are compared with laser-induced incandescence and Raman spectra observed from samples thermophoretically-extracted using a rapid insertion technique. In some flame regions, the Raman spectra were obscured by intense radiation that appeared to peak in the near infrared spectral region. We refer to this as *ex situ*, laser-induced incandescence (ES-LII). There is good agreement between the spatial profiles of this signal and the “traditional” *in situ* laser-induced incandescence (IS-LII).

Raman signatures were observed from very low in the flame and extended into the upper visible flame regions. The spectra consisted of overlapping bands between 1000 and 2000  $\text{cm}^{-1}$  dominated by the “G” band, near  $\approx 1580 \text{ cm}^{-1}$ , and the “D” band in the upper 1300  $\text{cm}^{-1}$  range. A variety of routines are explored to fit the data including 3-band and 5 band models, which deconvolve the “D” band into components, and a 2-band Breit–Wigner–Fano (BWF) model. Because the Raman signals were observed at heights below those where in situ-LII was observed, we postulate that these signals may be attributable to smaller particles. The ratio of the “D” to “G” band intensities is used to estimate the crystallite size,  $L_a$ . This quantity varies only slightly in all of the data and is estimated to be  $\approx 1.0\text{--}1.2 \text{ nm}$ . The results suggest that the observed Raman signals are attributable to particulate with modest-sized  $\pi$  conjugation lengths that would be expected for clusters of PAH with individual masses between  $\approx 500$  and 1000 Da. This observation is discussed in the context of current models for nascent particle formation.

## Acknowledgments

This material is based upon work supported by the National Science Foundation under Grant No. CBET-0828950 and Yale Grant No. CBET-0828802 with Drs. Philip Westmoreland and Arvind Atreya serving as technical monitors. Grant in Kind support from Thorlabs, Kaiser Optical Systems, and MD Anderson Cancer Center are also gratefully acknowledged.

## Appendix A. Supplementary data

Supplementary data associated with this article can be found, in the online version, at doi:10.1016/j.carbon.2011.07.050.

## REFERENCES

- [1] H.G. Wagner, Soot Formation in Combustion. Symposium (International) on Combustion 17 (1979) 3–19.
- [2] Cain JP, Gassman PL, Wang H, Laskin A. Micro-FTIR study of soot chemical composition-evidence of aliphatic hydrocarbons on nascent soot surfaces. *Physical Chemistry Chemical Physics* 2010;12:5206–18.
- [3] Schuetz CA, Frenklach M. Nucleation of Soot: Molecular Dynamics Simulations of Pyrene Dimerization. *Proceedings of the Combustion Institute* 2002;29:2307–14.
- [4] Miller JH. The kinetics of polynuclear aromatic hydrocarbon agglomeration in flames. *Proceedings of the Combustion Institute* 1991;23:91–89.
- [5] Miller JH. Aromatic Excimers: Evidence for Polynuclear Aromatic Hydrocarbon Condensation in Flames. *Proceedings of the Combustion Institute* 2005;30:1381–8.
- [6] Happold J, Grotheer H-H, Aigner M. Distinction of gaseous soot precursor molecules and soot precursor particles through photoionization mass spectrometry. *Rapid Communications in Mass Spectrometry* 2007;21(7):1247–54.
- [7] Violi A. Modeling of soot particle inception in aromatic and aliphatic premixed flames. *Combustion and Flame* 2004;139(4):279–87.
- [8] Fiedler SL, Izvekov S, Violi A. The effect of temperature on nanoparticle clustering. *Carbon* 2007;45:1786–94.
- [9] Chung S-H, Violi A. Peri-condensed aromatics with aliphatic chains as key intermediates for the nucleation of aromatic hydrocarbons. *Proceedings of the Combustion Institute* 2011;33(1):693–700.
- [10] Tuinstra F, Koenig JL. Raman spectrum of graphite. *Journal of Chemical Physics* 1970;53(3):1126–30.
- [11] Sze SK, Siddique N, Sloan JJ, Escribano R. Raman spectroscopic characterization of carbonaceous aerosols. *Atmospheric Environment* 2000;35(3):561–8.
- [12] Rosen H, Hansen ADA, Gundel L, Novakov T. Identification of the optically absorbing component in urban aerosols. *Applied Optics* 1978;17(24):3859–61.
- [13] Blaha JJ, Rosasco GJ, Etz ES. Raman microprobe characterization of residual carbonaceous material associated with urban airborne particulates. *Applied Spectroscopy* 1978;32(3):292–7.
- [14] Dovbeshko GI, Gnatyuk OP, Dovbeshko GI, Nazarova AN, Sementsov YI, Obraztsova ED. Vibrational spectra of carbonaceous materials: a SEIRA spectroscopy versus FTIR and Raman. *Fullerenes Nanotubes and Carbon Nanostructures* 2005;13(Suppl. 1):393–400.
- [15] Ivleva NP, McKeon U, Niessner R, Poschl U. Raman microspectroscopic analysis of size-resolved atmospheric aerosol particle samples collected with an ELPI: soot, humic-like substances, and inorganic compounds. *Aerosol Science and Technology* 2007;41:655–71.
- [16] Potgieter-Vermaak SS, Van Grieken R. Preliminary evaluation of micro-Raman spectrometry for the characterization of individual aerosol particles. *Applied Spectroscopy* 2006;60(1):39–47.
- [17] Beyssac O, Goffe B, Chopin C, Rouzaud J-N. Raman spectra of carbonaceous material in metasediments: a new geothermometer. *Journal of Metamorphic Geology* 2002;20:859–71.
- [18] Pasteris JD, Wopenka B. Necessary, but not sufficient: Raman identification of disordered carbon as a signature of ancient life. *Astrobiology* 2003;3(4):727–38.
- [19] Brunetto R, Pino T, Dartois E, Cao A-T, d’Hendecourt L, Strazzulla G, et al. Comparison of the Raman spectra of ion irradiated soot and collected extraterrestrial carbon. *Icarus* 2009;200:323–37.
- [20] Bouhadda Y, Bormann D, Sheu E, Bendedouch D, Krallafa A, Daaou M. Characterization of Algerian Hassi-Messaoud asphaltene structure using Raman spectrometry and X-ray diffraction. *Fuel* 2007;86(12–13):1855–64.
- [21] Yan S, Jiang Y-J, Marsh ND, Eddings EG, Sarofim AF, Pugmire RJ. Study of the evolution of soot from various fuels. *Energy & Fuels* 2005;19:1804–11.
- [22] Ivleva NP, Messerer A, Yang X, Niessner R, Poschl U. Raman Microspectroscopic Analysis of Changes in the chemical structure and reactivity of soot in a diesel exhaust aftertreatment model system. *Environmental Science and Technology* 2007;41:3702–3.
- [23] Sadezky A, Muckenhuber H, Grothe H, Niessner R, Poeschl U. Raman microspectroscopy of soot and related carbonaceous materials. Spectral analysis and structural information. *Carbon* 2005;43(8):1731–42.
- [24] Knauer M, Carrara M, Rothe D, Niessner R, Ivleva NP. Changes in structure and reactivity of soot during oxidation and gasification by oxygen, studied by micro-Raman spectroscopy and temperature programmed oxidation. *Aerosol Science and Technology* 2009;43(1):1–8.
- [25] Escribano R, Sloan JJ, Siddique N, Sze N, Dudev T. Raman spectroscopy of carbon-containing particles. *Vibrational Spectroscopy* 2001;26(2):179–86.
- [26] Sheng C. Char structure characterized by Raman spectroscopy and its correlations with combustion reactivity. *Fuel* 2007;86(15):2316–24.

- [27] Dippel B, Jander H, Heintzenberg J. NIR FT Raman spectroscopic study of flame soot. *Physical Chemistry Chemical Physics* 1999;1(20):4707–12.
- [28] Sadezky A, Muckenhuber H, Grothe H, Niessner R, Schlögl U. Raman microspectroscopy of soot and related carbonaceous materials: spectral analysis and structural information. *Carbon*. 2005;43:1731–42.
- [29] Ivleva NP, Messerer A, Yang X, Niessner R, Poschl U. Raman microspectroscopic analysis of changes in the chemical structure and reactivity of soot in a diesel exhaust aftertreatment model system. *Environmental Science and Technology* 2007;41:3702–7.
- [30] Castiglioni C, Mapelli C, Negri F, Zerbi G. Origin of the D line in the Raman spectrum of graphite: a study based on Raman frequencies and intensities of polycyclic aromatic hydrocarbon molecules. *Journal of Chemical Physics* 2001;114(2):963–74.
- [31] Yoshida A, Kaburagia Y, Hishiyama Y. Full width at half maximum intensity of the G band in the first order Raman spectrum of carbon material as a parameter for graphitization. *Carbon* 2006;44(11):2333–5.
- [32] Lespade P, Marchand A. Caractérisation de matériaux carbonés par microspectrométrie Raman. *Carbon* 1984;22:375–85.
- [33] Dresselhaus MS, Dresselhaus G. Light scattering in graphite intercalation compounds. In *Light scattering in solids III*. In: *Topics in applied Physics*, vol. 51; 1982. p. 3–57.
- [34] Cuesta A, Dhamelincourt P, Laureyns J, Martínez-Alonso A, Tascon JMD. Raman microprobe studies on carbon materials. *Carbon* 1994;32(8):1523–32.
- [35] Jawhari T, Roid A, Casado J. Raman spectroscopic characterization of some commercially available carbon black materials. *Carbon* 1995;33(11):1561–5.
- [36] Sze SK, Siddique N, Sloan JJ, Escribano R. Raman spectroscopic characterization of carbonaceous aerosols. *Atmospheric Environment* 2000;35(3):561–8.
- [37] Dippel B, Heintzenberg J. Soot characterization in atmospheric particles from different sources by NIR FT Raman spectroscopy. *Journal of Aerosol Science* 1999;30(Supplement 1):S907–8.
- [38] Ferrari AC, Robertson J. Interpretation of Raman spectra of disordered and amorphous carbon. *Physical Review B: Condensed Matter and Materials Physics* 2000;61(20):14095–107.
- [39] Cancado LG, Takai K, Enoki T, Endo M, Kim YA, Mizusaki H, et al. General equation for the determination of the crystallite size  $L_a$  of nanographite by Raman spectroscopy. *Applied Physics Letters* 2006;88:1631061–3.
- [40] Ferrari AC, Robertson J. Resonant Raman spectroscopy of disordered amorphous and diamond like carbon. *Physical Review B* 2001;64:075414-1–13.
- [41] Negri F, Di Donato E, Tommasini M, Castiglioni C, Zerbi G. K.M. Resonance Raman contribution to the D band of carbon materials: Modeling defects with quantum chemistry. *Journal of Chemical Physics* 2004;120(24):11889–900.
- [42] Knight DS, White WB. Characterization of diamond films by Raman spectroscopy. *Journal of Materials Research* 1989;4(2):385–93.
- [43] Matthews MJ, Pimenta MA, Dresselhaus G, Dresselhaus MS, Endo M. Origin of dispersive effects of the Raman D band in carbon materials. *Physical Review B* 1999;59(10):R6585–8.
- [44] Zickler GA, Smarsly B, Gierlinger N, Peterlik H, Paris O. A reconsideration of the relationship between the crystallite size  $L_a$  of carbons determined by X-ray diffraction and Raman spectroscopy. *Carbon* 2006;44(15):3239–46.
- [45] Lucchese MM, Stavale F, Ferreira EHM, Vilani C, Moutinho MVO, Capaz RB, et al. Quantifying ion-induced defects and Raman relaxation length in graphene. *Carbon* 2010;48:1592–7.
- [46] Cancado LG, Jorio A, Pimenta MA. Measuring the absolute Raman cross section of nanographites as a function of laser energy and crystallite size. *Physical Review B* 2007;76:0643031–7.
- [47] L.G. Cancado, A. Jorio, E.H.M. Ferreira, F. Stavale, C.A. Achete, R. Capaz et al., Quantifying Defects in Graphene via Raman Spectroscopy at Different Excitation Energies, *Nano Letters* 2011. doi:10.1021/nl201432g
- [48] Mewes B, Seitzman JM. Soot volume fraction and particle size measurements with laser-induced incandescence. *Applied Optics* 1997;36(3):709–17.
- [49] Quay B, Lee TW, Ni T, Santoro RJ. Spatially-resolved measurements of soot volume fraction using laser-induced incandescence. *Combustion and Flame* 1994;97(3–4):384–92.
- [50] Zhao H, Ladommatos N. Optical diagnostics for soot and temperature measurement in diesel engines. *Progress in Energy and Combustion Science* 1998;24(3):221–55.
- [51] Vander Wal RL, Welland KJ. Laser-induced incandescence. Development and characterization towards a measurement of soot-volume fraction. *Applied Physics B* 1994;59:445–52.
- [52] Axelsson B, Collin R, Bengtsson PE. Laser-induced incandescence for soot particle size and volume fraction measurements using on-line extinction calibration. *Applied Physics B-Lasers and Optics* 2001;72(3):367–72.
- [53] B.C. Connelly, Quantitative Characterization of Steady and Time-Varying Sooting, Laminar Diffusion Flames using Optical Techniques, Yale University, Ph.D., 2009.
- [54] Krishnan SS, Lin KC, Faeth GM. Extinction and scattering properties of soot emitted from buoyant turbulent diffusion flames. *Journal of Heat Transfer-Transactions of the ASME* 2001;123(2):331–9.
- [55] Williams TC, Shaddix CR, Jensen KA, Suo-Anttila JM. Measurement of the dimensionless extinction coefficient of soot within laminar diffusion flames. In: *Fourth joint meeting of the U.S. sections of the combustion institute: western states, central states, eastern states*. Philadelphia, PA, United States; 2005. p. A14-1–6.
- [56] Dobbins RA, Megaridis CM. Morphology of flame-generated soot as determined by thermophoretic sampling. *Langmuir* 1987;3(2):254–9.
- [57] Cundy VA, Morse JS, Senter DW. Constant-tension thermocouple rake suitable for use in flame mode combustion studies. *Review of Scientific Instruments* 1986;57(6):1209–10.
- [58] Lee J, Altman I, Choi M. Design of thermophoretic probe for precise particle sampling. *Journal of Aerosol Science* 2008;39(5):418–31.
- [59] Bennett BA, Fielding J, Mauro RJ, Long MB, Smooke MD. A comparison of the structures of lean and rich axisymmetric laminar Bunsen flames: application of local rectangular refinement solution-adaptive gridding. *Combustion Theory and Modelling* 1999;3(4):657–87.
- [60] Dworkin SB, Bennett BAV, Smooke MD. A mass-conserving vorticity-velocity formulation with application to nonreacting and reacting flows. *Journal of Computational Physics* 2005;215:430–47.
- [61] Ern A, Smooke MD. Vorticity-velocity formulation for 3-dimensional steady compressible flows. *Journal of Computational Physics* 1993;105:58–71.
- [62] Coffee TP, Heimerl JM. Transport algorithms for premixed, laminar, steady-state flames. *Combustion and Flame* 1981;43:273–89.
- [63] Kee RJ, Rupley FM, Miller JA. *The Chemkin Thermodynamic Database*. Livermore, CA: Sandia National Laboratories; 1987.
- [64] Kee RJ, Miller JA, Jefferson TH. *Chemkin: A General Purpose, Problem Independent, Transportable, Fortran Chemical*

- Kinetics Code Package. In: Facility CR, editor. Livermore CA: Sandia National Laboratories; 1980.
- [65] Kee RJ, Dixon-Lewis G, Warnatz J, Coltrin ME, Miller JA. A Fortran Computer Code Package for the Evaluation of Gas-Phase Multicomponent Transport Properties. Livermore, CA: Sandia National Laboratories; 1986.
- [66] Kee RJ, Warnatz J, Miller JA. A Fortran Computer Code Package for the Evaluation of Gas-Phase Viscosities, Conductivities, and Diffusion Coefficients. Livermore, CA: Sandia National Laboratories; 1983.
- [67] V. Giovangigli, N. Darabiha, Vector Computers and Complex Chemistry Combustion, in: C. Brauner, C. Schmidt-Lainé (Eds.), *Mathematical Modeling in Combustion and Related Topics*: M. Nijhoff NATO ASI Series, vol. 140, 1988, pp. 491–503.
- [68] Gelbard F, Seinfeld JH. Simulation of Multicomponent Aerosol Dynamics. *Journal of Colloid and Interface Science* 1980;78:485–501.
- [69] Gelbard F, Tambour Y, Seinfeld JH. Sectional Representation for Simulating Aerosol Dynamics. *Journal of Colloid and Interface Science* 1980;76:541–56.
- [70] Smooke MD, Long MB, Connelly BC, Colket MB, Hall RJ. Soot formation in laminar diffusion flames. *Combustion and Flame* 2005;143(4):613–28.
- [71] Dworkin SD, Smooke MD, Giovangigli V. The Impact of Detailed Multicomponent Transport and Thermal Diffusion Effects on Soot Formation in Ethylene/Air Flames. *Proceedings of the Combustion Institute* 2009;32:1165–72.
- [72] Smooke MD, McEnally CS, Pfefferle LD, Hall RJ, Colket MB. Computational and experimental study of soot formation in a coflow, laminar diffusion flame. *Combustion and Flame* 1999;117:117–39.
- [73] Smooke MD, Hall RJ, Colket MB, Fielding J, Long MB, McEnally CS, et al. Investigation of the transition from lightly sooting towards heavily sooting co-flow ethylene diffusion flames. *Combustion. Theory and Modelling* 2004;8:593–606.
- [74] McEnally CS, Shaffer AM, Long MB, Pfefferle LD, Smooke MD, Colket MB, et al. laminar ethylene diffusion flame. *Proceedings of the Combustion Institute* 1998;27(1):1497–505.
- [75] Harris SJ, Weiner AM. Soot particle growth in premixed toluene/ethylene flames. *Combustion Science and Technology* 1984;38(1–2):75–87.
- [76] Hura HS, Glassman I. Soot formation in diffusion flames of fuel/oxygen mixtures. *Symposium (International) on Combustion* 1989;22(1):371–8.
- [77] Sun CJ, Sung CJ, Wang H, Law CK. On the structure of nonsooting counterflow ethylene and acetylene diffusion flames. *Combustion and Flame* 1996;107(4):321–35.
- [78] Stein SE, Fahr A. High-Temperature Stabilities of Hydrocarbons. *Journal of Physical Chemistry* 1985;89:3714–25.
- [79] Faccinetto A, Desgroux P, Ziskind M, Therssen E, Focsa C. High-sensitivity detection of polycyclic aromatic hydrocarbons adsorbed onto soot particles using laser desorption/laser ionization/time-of-flight mass spectrometry: An approach to studying the soot inception process in low-pressure flames. *Combustion and Flame* 2011;158(2):227–39.
- [80] Dobbins RA, Fletcher RA, Chang HC. The evolution of soot precursor particles in a diffusion flame. *Combustion and Flame* 1998;115(3):285–98.
- [81] Jäger C et al. Formation of Polycyclic Aromatic Hydrocarbons and Carbonaceous Solids in Gas-Phase Condensation Experiments. *The Astrophysical Journal* 2009;696(1):706.
- [82] Miller JH. Aromatic eximers: evidence for polynuclear aromatic hydrocarbon condensation in flames. *Proceedings of the Combustion Institute* 2005;30:1381–8.
- [83] Frenklach M. Reaction mechanism of soot formation in flames. *Physical Chemistry Chemical Physics* 2002;4:2028–37.
- [84] Brunetto R, Pino T, Dartois E, Cao A-T, d’Hendecourt L, Strazzulla G, et al. Comparison of the Raman spectra of ion irradiated soot and collected extraterrestrial carbon. *Icarus* 2009;200(1):323–37.
- [85] Ivleva NP, McKeon U, Niessner R, Poeschl U. Raman microspectroscopic analysis of size-resolved atmospheric aerosol particle samples collected with an ELPI: soot, humic-like substances, and inorganic compounds. *Aerosol Science and Technology* 2007;41(7):655–71.
- [86] Zeng H, Yang C, Dai J, Cui X. Light-induced incandescence of single-walled carbon nanotubes. *Journal of Physical Chemistry C* 2008;112(11):4172–5.
- [87] Frenklach M, Wang H. Detailed modeling of soot particle nucleation and growth. *Proceedings of the Combustion Institute* 1998;23:1559–66.
- [88] Herdman JD, Miller JH. Intermolecular potential calculations for polynuclear aromatic hydrocarbon clusters. *Journal of Physical Chemistry A* 2008;112(28):6249–56.
- [89] Totton TS, Chakrabarti D, Misquitta AJ, Sander M, Wales DJ, Kraft M. Modelling the internal structure of nascent soot particles. *Combustion and Flame* 2010;157(5):909–14.
- [90] Sander M, Patterson RIA, Braumann A, Raj A, Kraft M. Developing the PAH-PP soot particle model using process informatics and uncertainty propagation. *Proceedings of the Combustion Institute* 2011;33(1):675–83.